LAWRENCE
LIVERMORE
NATIONAL
LABORATORY

UCRL-CONF-225774

Experiment on mass-stripping of interstellar cloud following shock passage

J. F. Hansen, H. F. Robey, R. I. Klein, A. R. Miles

November 1, 2006

48th Meeting of the Division of Plasma Physics
Philadelphia, PA, United States
October 30, 2006 through November 3, 2006

Disclaimer

Not to appear in Nonlearned J., 45.

Experiment on mass-stripping of interstellar cloud following shock passage

J. F. Hansen and H. F. Robey and R. I. Klein [1] and A. R. Miles

Lawrence Livermore National Laboratory, Livermore CA 94550

hansen46@llnl.gov

ABSTRACT

The interaction of supernova shocks and interstellar clouds is an important astrophysical phenomenon which can lead to mass-stripping (transfer of material from cloud to surrounding flow, "mass-loading" the flow) and possibly increase the compression in the cloud to high enough densities to trigger star formation. Our experiments attempt to simulate and quantify the mass-stripping as it occurs when a shock passes through interstellar clouds. We drive a strong shock using 5 kJ of the 30 kJ Omega laser into a cylinder filled with low-density foam with an embedded 120 μm Al sphere simulating an interstellar cloud. The density ratio between Al and foam is ~ 9. Time-resolved x-ray radiographs show the cloud getting compressed by the shock ($t \approx 5$ ns), undergoing a classical Kelvin-Helmholtz roll-up (12 ns) followed by a Widnall instability (30 ns), an inherently 3D effect that breaks the 2D symmetry of the experiment. Material is continuously being stripped from the cloud at a rate which is shown to be inconsistent with laminar models for mass-stripping (the cloud is fully stripped by 80 ns-100 ns, ten times faster than the laminar model). We present a new model for turbulent mass-stripping that agrees with the observed rate and which should scale to astrophysical conditions, which occur at even higher Reynolds numbers than the current experiment. The new model combines the integral momentum equations, potential flow past a sphere, flat plate skin friction coefficients, and Spalding's law of the wall for turbulent boundary layers.

Subject headings: ISM: clouds — ISM: kinematics and dynamics — hydrodynamics — shock waves — turbulence — instabilities

---

[1] Department of Astronomy, University of California, Berkeley CA 94720

1. Introduction

Observations of astronomical media show that condensations embedded in more diffuse plasma is a common phenomenon. The flows present in the surrounding diffuse material can be initiated and enhanced by the injection of energy and momentum from supernovae, stellar winds, mass loss from active galactic nuclei and possible mass loss from galaxy clusters. Mass-loading is thought to be important in the Wolf-Rayet wind-blown bubble RCW 58 (Smith et al. 1984) as well as the winds from T-Tauri type stars and other young stars and occurs from the ablation of molecular clumps of gas by these winds creating high velocity flows. The flow surrounding condensations results in pressure gradients across its surface, dissipation and acceleration to the flow velocity. Mass-loading, the transport of matter from the condensation into the flow can indeed alter the structure of the flow itself. Although the process of mass-loading is an important occurrence in nearly all astrophysical flows, the experimental study of such flows is still in an early stage of development. Early theoretical work on mass exchange concentrated on conduction fronts between cold material and more diffuse static plasma (Cowie et al. 1981). These descriptions are not strictly applicable to finite Mach number flows in turbulent media. Theoretical work on mass-loaded flows due in particular to mass-loaded winds has been done by Hartquist et al. (1986). Flows driven by mass-loading may occur on all astronomical scales (Hartquist et al. 1986) and may have important effects on scales ranging from galactic winds interacting with inhomogeneities in the early universe to winds from clusters of galaxies or starburst galaxies ablating very large-scale perturbations (Marcolini et al. 2005).

Woodward (1976) and Nittmann et al. (1982) have studied the interaction of a supernova shock with an initially pressure-confined cloud. Heathcote & Brand (1983) described the main features of this interaction after the passage of the shock. Shocks passing through interstellar clouds can trigger star formation or increase the star formation rate, but also limit the time over which star formation is possible (Hartmann et al. 2001). Recent analyses (Palla & Stahler 2000) suggest that clouds are relatively short-lived (average age a few million years). The interaction may seed turbulence in the clouds, believed to play an important role in the fragmentation of the clouds (Padoan et al. 2001; Clark & Bonnell 2005) and in the star formation process (Larson 1981). Shock-cloud interactions have been seen in several astrophysical objects, e.g., the Cygnus loop (Bedogni & Woodward 1990; Patnaude & Fesen 2005), the Vela supernova remnant (SNR) (Miceli et al. 2005), SNR HB 21(Byun et al. 2006) , just to mention a few, and may play an important role for the evolution of clouds and for star formation everywhere from the solar neighborhood (Hartmann et al. 2001) to intergalactic clouds (Fragile et al. 2004). (We also note that the situation with a cloud being stripped of its mass through a turbulent boundary layer has some similarity to a meteorite falling through the Earth's atmosphere, or the solar wind ablating a comet, although in these

cases the core of the ablated object remains solid.)

Klein et al. (1994, 2000) performed a comprehensive study of the shock-cloud interaction using high resolution adaptive mesh refinement 2-D hydrodynamics, developed the theory for each stage of the interaction with detailed comparisons with their simulations, and also performed the first scaled laser experiments investigating the interaction of a supernova shock with an interstellar cloud. The experiments were initially performed at the Nova laser facility (Klein et al. 2000) and later at the Omega facility (Robey et al. 2002; Klein et al. 2003). The results of these experiments were compared in detail to the numerical simulations and the theoretical work and showed excellent agreement with the simulations for most stages of the interaction. The experiments were among the first to demonstrate the long term behavior of compressible clouds immersed in supersonic flow. Recently, shock-cloud interaction evolved to a late time was observed and identified by Hwang et al. (2005) in SNR Puppis A by comparing morphological features in observational and experimental images.

Beyond morphology, experiments may also give some quantitative measure on turbulence, and in this paper we present the results of a continued set of laser experiments designed to study the interaction between a supernova shock and an interstellar cloud, including a new model for turbulent mass-stripping (transfer of material from cloud to surrounding flow, mass-loading the flow) that is in good agreement with the experimentally observed rate and which should scale to astrophysical conditions. The experiments were carried out at the Omega laser at the Laboratory of Laser Energetics in Rochester, New York (Boehly et al. 1997).

2. Experimental setup and diagnostics

The strong shock (and blast wave) of a supernova explosion is simulated at experiments at Omega in the following manner: a small beryllium shock tube (2.25 mm long; 0.8 mm inner diameter; 1.1 mm outer diameter) is filled with a low density (300 mg/cm^3) carbonized resorcinol formaldehyde foam (CRF). The CRF at one end of the shock tube is then ablated by laser beams, causing the ejection of ablated material in one direction to launch a planar shock in the opposite direction. Good planarity of the shock is ensured by using multiple (ten), superimposed beams, each with a super-gaussian beam profile created by a phase plate in the focusing optics; the super-gaussian is $\exp\left[-\left(r/d\right)^n\right]$ with $n = 4.7$ and $d = 430$ μm; the beam angles of incidence were 10.3° (one beam), 31.7° (three beams), 42.2° (four beams), and 50.5° (two beams). Each laser beam has an energy of ~ 500 J with a pulse duration of 1.0 ns. Note that after the laser beams are turned off, a rarefaction follows the shock into shock tube, so the shock soon develops into a blast wave. Figure 1 shows the experimental

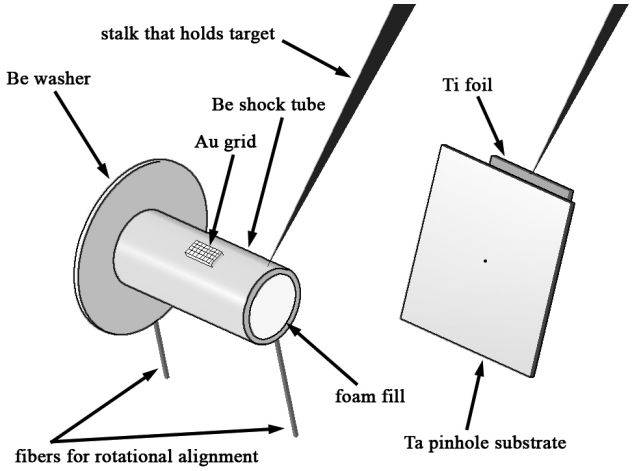

Fig. 1.— Experimental set-up. A beryllium shock tube is filled with a low density foam and is open at both ends. A small aluminum sphere is embedded in the foam (inside the shock tube and not visible in this drawing). The experiment starts when ten laser beams launches a shock in the foam from one end of the shock tube. The shock develops into a blast wave and propagates through the shock tube and interacts with the embedded sphere. The evolution of the sphere is recorded by an x-ray camera (far outside the field of view of this drawing). X rays for the camera are generated by additional laser beams striking a titanium foil. The x rays can be focused either by a pinhole in the camera or by a pinhole in a tantalum substrate that is placed immediately adjacent to the Ti foil. A gold grid mounted on the outside surface of the shock tube provides a spatial reference in the x-ray images.

set-up.

Physical quantities in the CRF can be accurately calculated using the hydrodynamic code HYADES. [This a 1D Lagrangean hydrodynamics and energy transport code where electron and ion components are treated separately in a fluid approximation, each in thermodynamic equilibrium and described by Maxwell-Boltzmann statistics, but loosely coupled to each other. Radiation is coupled only to the electron fluid and is assumed (in our calculations) Planckian and treated as single-group (grey approximation). All energy transport is modeled using the diffusion approximation. For further information on the HYADES code refer to Larsen & Lane (1994).] We have used HYADES to calculate the free-stream velocity $U_\infty(t)$, the temperature $T(t)$, the Mach number $M(t)$, and the density $\rho_1(t)$ for the CRF and these quantities are plotted in Fig. 2. The simulation used an in-line quotidian equation of state model [QEOS; an equation of state model based on Thomas-Fermi physics (More et al. 1988)] with a bulk modulus of 3×10^9 Pa and 112 zones to represent the 2.25 mm long CRF, with

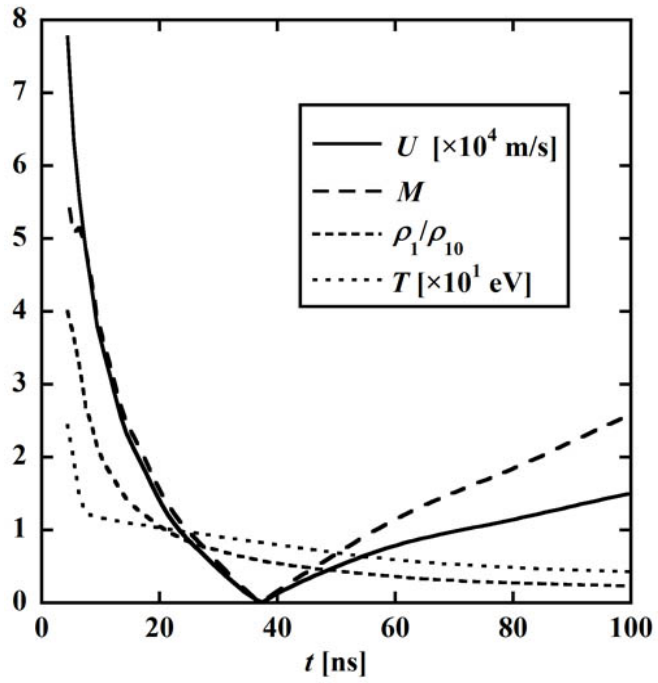

Fig. 2.— HYADES calculation of the free-stream velocity $U_\infty = U_\infty(t)$, the Mach number $M(t)$, the compression $\rho_1(t)/\rho_{10}$ (where the initial density $\rho_{10} = 300$ mg/cm^3), and the temperature $T = T(t)$.

the first 46 zones feathered for ablation with a zone-to-zone scaling ratio of 1.15, the final 46 zones feathered for shock release with a scaling ratio of 0.87. The laser energy in the simulation was tuned to match shock velocities with experimental data. This tuning of the simulation compensates for loss of energy in the experiments due to lateral expansion of shock tube walls, laser-plasma interaction, preheating of the CRF, etc. [Note that the CRF may be more compressible than what the QEOS allows for, meaning at a given energy a shock in the experiment would move slower than in the numerical simulation. Then when we reduce the simulation energy to match the shock position with the real shock position, we end up with a simulation with a slower than real flow speed. However, this change is fairly small - likely smaller than that of the six times less dense CRF (50 mg/cm^3) used in Miles et al. (2004) - and is assumed negligible.]

The scaled ISM cloud is simulated by an aluminum sphere (radius $R_0 = 60$ μm) embedded in the CRF a short distance into the shock tube (on the shock tube axis 500 μm from the ablated CRF surface). The density ratio between the Al (density 2.7 g/cm^3) and the surrounding CRF is chosen to match the density ratio χ for an actual ISM cloud [$\chi \sim 10 - 100$

(Klein et al. 1994)] and other experimental parameters are also scaled to preserve the physics regime of the astrophysical case. In particular, a flow described by the Euler equations will remain governed by the Euler equations after a parameter-scaling if the following four criteria (Ryutov et al. 1999) are satisfied: (1) Particles are localized on spatial scales smaller than the characteristic length scale D_0 of the system, e.g., the collisional mean free path $\lambda_c \ll D_0$. (2) Convective (hydrodynamic) transport must dominate particle (heat) conduction, e.g., the Peclet number Pe $\gg 1$ so that the travel time at the speed of sound over a characteristic length scale is shorter than the thermal or radiative conductive times. (3) Energy fluxes carried by the flow (hydrodynamics) must be large compared to radiative energy fluxes. (4) Viscous dissipation needs to be small compared to inertial forces, i.e., the Reynolds number Re $\gg 1$. [In addition to these four criteria, the flow is assumed to be non-magnetic and we also note that while the blast-wave width likely has some impact on the evolution of the cloud, it is unlikely to affect the final conclusions of this manuscript simply because the blast-wave width is no larger than the cloud dimension (we estimate it at < 90 μm from the HYADES simulation), and, as we shall see, the mass-stripping is due to the cloud's exposure to a surrounding flow for an extended period of time, not only at the moment the blast-wave passes. Had the blast-wave width been much larger than the cloud dimension, this situation would have been different.] We now demonstrate that the above four conditions are satisfied (at all times, by using a "worst" choice for parameters that fluctuate in time):

(1) The collisional mean free path (Ryutov et al. 1999): $\lambda_c \approx (8\times10^{-12}\ \mathrm{cm^{-6}s^4})\times U^4/\Lambda n$, where the velocity $U \leqslant 77$ km/s in our experiment, estimated from numerical simulations (see below), the coulomb logarithm $\Lambda \approx 6$ within a factor of a few, and the ion number density $n = 1.5 \times 10^{28}$ m^{-3} in the CRF (which consists of 93% C, 6% O, and 1% H by weight). We then calculate $\lambda_c \approx 3 \times 10^{-9}$ m which is considerably smaller than the characteristic length scale $D_0 = 2R_o = 1.2 \times 10^{-4}$ m. (The mean free path in the Al sphere is even smaller due to its higher density.)

(2) The Peclet number Pe $= D_0 U/\chi$ where we should now use the estimated (see below) lower limit for the velocity, $U \geqslant 1$ km/s, and where the electron thermal diffusivity (Ryutov et al. 1999) is $\chi = (1.4\times10^{11}\ \mathrm{cm^{-1}s^{-1}K^{-5/2}})\times T^{5/2}/\Lambda n Z\,(Z+1)$. With $T \geqslant 5$ eV estimated from numerical simulations (see below) and an averaged atomic number $Z = 6.07$ for the foam we calculate Pe $= 1.3 \times 10^4 \gg 1$.

(3) For an optically thick plasma like the Al cloud, to show that energy fluxes carried by the flow are large compared to radiative energy fluxes, it suffices to show that the radiative cooling time τ_B (estimated from blackbody radiation) is long compared to the characteristic hydrodynamical timescale τ_h. For the Al sphere (Ryutov et al. 1999): $\tau_B = (1.9 \times 10^{-12}\ \mathrm{cm^2sK^3}) \times (Z+1)\, nD_0/T^3$. The density and temperature of course

changes with time, but even a worst case choice of $n = 6.0 \times 10^{28}$ m^{-3} (which assumes no compression) and $T \approx 10$ eV (the highest estimated temperature from numerical simulations) satifies the criteria as we then calculate $\tau_B \approx 1.2 \times 10^{-5}$ s which is much longer than the characteristic time scale $\tau_h = D_0/U \leqslant 1.2 \times 10^{-7}$ s. For the CRF this simple estimate is not sufficient (because $\tau_h \sim \tau_B$), so we need to calculate a radiative Peclet number $\mathrm{Pe}_\gamma = D_0 v/\chi_\gamma$ and show that this is much greater than unity. We have $\chi_\gamma = \kappa_\gamma/c_V$ where the specific heat $c_V = 16\sigma T^3/c + 3\,(Z+1)\,nk_B/2$ and where the radiative thermal conductivity $\kappa_\gamma = 16\lambda\sigma T^3/3$ is calculated from the smaller of the Rosseland and Thompson mean free paths. These are (Ryutov et al. 1999): $\lambda_R = (1.0 \times 10^{23}\ \mathrm{cm}^{-5}\mathrm{K}^{7/2}) \times T^{7/2}/Z^3 n^2 = 1 \times 10^{-8}$ m and $\lambda_T = (2.5\ \mathrm{cm}^{-2}\mathrm{g}) \times A/Z\rho = 0.5$ m in our case. We then calculate $\mathrm{Pe}_\gamma = 5 \times 10^4 \gg 1$. (Since the radiative Peclet number is related to the Boltzmann number $\mathrm{Bo} = Uc_V T/\sigma T^4$ by $\mathrm{Pe}_\gamma = 3D_0\mathrm{Bo}/16\lambda$ one could instead show that $\mathrm{Bo} > 1$ since in this case $D_0 \gg \lambda$. Using the values above $\mathrm{Bo} \approx 25$.)

(4) The Reynolds number $\mathrm{Re} = D_0 U/\nu$ where the kinematic viscosity ν strictly speaking must include both photon viscosity and particle viscosity (although we expect the particle viscosity to dominate). The photon viscosities are easily calculated (Ryutov et al. 1999) from $\nu_{photon} = (1.7 \times 10^{-25}\ \mathrm{cm}^{-4}\mathrm{g}^2\mathrm{s}^{-1}\mathrm{K}^{-4}) \times AT^4/Z\rho^2$ and for $T \approx 10$ eV we get $\nu_{photon} = 6.8 \times 10^{-8}$ m^2/s for the CRF and $\nu_{photon} = 8.8 \times 10^{-10}$ m^2/s for the Al cloud. The particle viscosity is more complicated as the plasma coupling parameter $\Gamma > 1$, i.e., the Braginskii viscosity for weakly coupled plasma ions is invalid. We must use the more extensive viscosity model by Clérouin et al. (1998); Robey (2004): $\nu_{particle} = (6.55 \times 10^{-10}\ \mathrm{cm}^{9/2}\mathrm{s}^{-1}\mathrm{g}^{-1/2}) \times Zm_i^{1/2} n^{5/6} \left(\lambda I_1 + (1+\lambda I_2)^2/\lambda I_3\right)$ where m_i is the ionic mass and the parameters λ, I_1, I_2, and I_3 are calculated from the plasma coupling parameter $\Gamma = Z^{1/3} \sum_j (x_j Z_j)\, q_e^2\, (4\pi/3 \times n)^{1/3}/4\pi\varepsilon_0 k_B T$ where x_j is the mass fraction of the j^{th} ionic species with atomic number Z_j. The parameters are: $\lambda = 4\pi\,(3\Gamma)^{3/2}/3$, $I_1 = \left(180\pi^{3/2}\Gamma\right)^{-1}$, $I_2 = \left(0.49 - 2.23\Gamma^{-1/3}\right)/60\pi^2$, and $I_3 = 2.41\Gamma^{1/9}/10\pi^{3/2}$. We then calculate $\nu_{particle} = 5.4 \times 10^{-7}$ m^2/s for the CRF and $\nu_{particle} = 1.5 \times 10^{-5}$ m^2/s for the Al cloud. The Reynolds number is then clearly above unity ($\mathrm{Re} \approx 8 \times 10^3$ in the Al cloud), and consequently all four criteria for a properly scaled experiment are satisfied, meaning the overall morphology of the cloud is properly scaled.

Preheating of the sphere could result in an expansion of the sphere radius prior to the shock reaching the sphere. We have checked this expansion using the Lawrence Livermore CALE code (Barton 1985) (an arbitrary Lagrangian-Eulerian code) and found that only the outermost 4 μm of the sphere are significantly affected by preheat. This is consistent with observed sphere expansion in the experimental images. The amount of sphere mass affected by preheat is thus relatively small, so even if this mass is stripped faster than what otherwise

would have been the case, it would not change the final conclusions of this manuscript.

The cloud is imaged using a gated x-ray framing camera (Budil et al. 1996). X rays for the image are generated by a second set of time-delayed laser beams (backlighter beams) pointed at a metal foil, typically titanium, located on the opposite side of the shock tube from the camera. These x rays (mainly He-α radiation at 4.7 keV) moves through the shock tube and is imaged by a 10 μm pinhole at the front end of the camera. (This is called "area radiography"; over the course of our experiments we also developed and used a more advanced imaging technique - "point projection radiography" - where the pinhole is located right next to the Ti foil and has a diameter of 20 μm.) The imaging element of the camera is either a microchannel plate (MCP) + film or MCP + charge coupled device (CCD), and in both cases has a size of $\sim$ 35 mm. The distance from shock tube to Ti foil is 4.0 mm (for area radiography, 6.5 mm for point projection radiography) and the imaging element is located to give a magnification such that the shock tube image roughly fills the imaging element. The time-delay for the backlighter beams is chosen to obtain an image at a desired time t after the initial, ablative laser pulse has started the shock in the shock tube. The camera MCP is triggered to coincide with the backlighter beams. The MCP pulse length was set to 500 ps in a trade-off between maximizing x-ray exposure on the MCP while minimizing motion blurring (e.g., when the plasma moves 20 km/s the motion blurring is 10 μm comparable to the pinhole diameter). The experiment is repeated with different time-delays to generate an image sequence.

3. Results

Results from the experiment can be seen in Fig. 3. As the shock runs over the cloud (t = 5 ns), its speed inside the cloud is greatly reduced. The velocity difference between surrounding flow and cloud material eventually leads to a Kelvin-Helmholtz instability and its characteristic roll-up (t = 12 ns). Soon thereafter, a Widnall-type instability (Widnall et al. 1974) occurs, creating a low mode number azimuthal perturbation of order five when viewed from a point on the extended shock tube axis (Robey et al. 2002; Klein et al. 2003). Here we see the Widnall instability as four "fingers" at the trailing edge of the cloud at t = 30 ns, indicating a mode number of four to eight (depending on if each finger is or is not overlapping another finger along the line of sight). Material is constantly being stripped away from the Al plasma cloud and is visible in the images as a cone of diffuse material behind the cloud ($t \geq$ 19 ns). By t = 40 ns this cone extends outside our diagnostic field of view. By t = 60 ns so much material has been stripped away that the remaining cloud is quite diffuse (we are showing the 60 ns image at a higher contrast than the earlier point

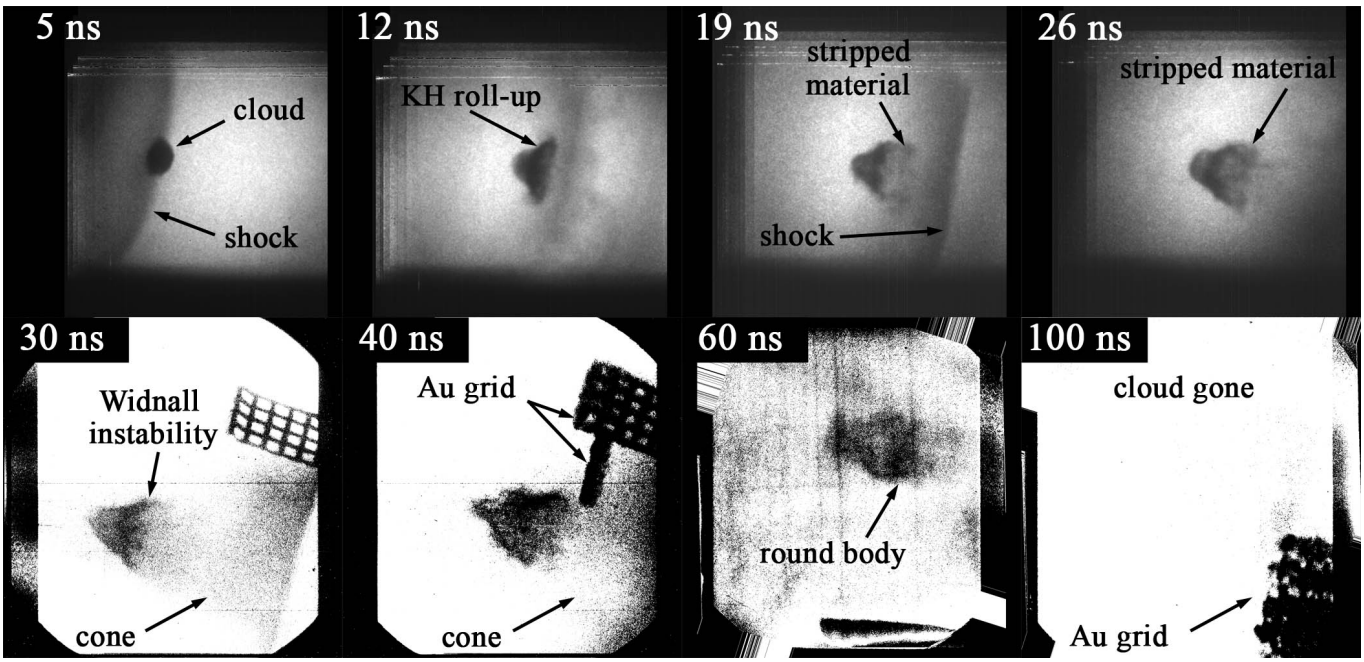

Fig. 3.— A time sequence of images showing how the cloud evolves after the passage of a shock (actually blast wave since a rarefaction follows the shock). In each image, the direction of motion of the shock is approximately from left to right, and is perpedicular to the imaged shock at time $t = 19$ ns, and the imaged Au grids at times $t = 30$ ns and 40 ns. In the first image, at $t = 5$ ns, the shock is intersecting the cloud and the left hand side of the cloud is compressed by a factor of 4, the strong shock limit for a polytropic gas with an adiabatic index $\gamma = 5/3$. The cloud undergoes a classical Kelvin-Helmholtz roll-up, as seen at $t = 12$ ns and later. Cloud material is stripped away from the cloud. Stripped material is clearly evident trailing the cloud at $t \geq 19$ ns and is shaped as a cone that extends all the way to the shock (or extends outside the field of view at $t = 40$ ns). The rarefaction changes the direction of the surrounding flow at approximately $t = 40$ ns, and by $t = 60$ ns the reverse flow has caused the right hand side of the cloud to become fairly round. By $t = 100$ ns the cloud has disappeared. The first four images were obtained with area backlighters, the last four with point projection radiography.

projection radiography images in Fig. Fig. 3). By $t = 100$ ns the cloud has been completely stripped away and can no longer be identified in the point projection radiography images. We also obtained an image at 80 ns in which the cloud is completely gone, but this target unfortunately had its gold spatial reference grid (c.f. Fig. 1) mounted outside the view of the x-ray framing camera and was therefore not included in Fig. 3.

To quantify how far out in time our experiment goes, allowing comparison to other experiments and numerical simulations, we estimate the cloud crushing time $t_{cc} = \sqrt{\rho_{20}/\rho_{10}} \times R_0/U_\infty$, where $\rho_{10} = 300$ mg/cm^3 is the initial CRF density and $\rho_{20} = 2.7$ g/cm^3 the initial Al density. For the current experiment this quantity $t_{cc} \approx 2.3$ ns. In the Nova experiments presented by Klein et al. (2000, 2003), the much longer $t_{cc} = 8.3$ ns gives about $5.3 \times t_{cc}$ for their latest image. The same dimensionless time is reached by 17 ns in our experiment, and we continue to take data out to over $30 \times t_{cc}$.

Because the point projection radiography technique illuminates the MCP in a very uniform fashion, we can use the point projection radiography images to estimate the cloud mass. Mass attenuation along the line of sight in an x-ray image can be expressed as $I = I_0 \exp(-\mu m/A)$ where I is the measured pixel intensity, I_0 is the x-ray source intensity (i.e., the intensity we would have expected to measure had there not been mass attenuation), m is the integrated line of sight mass, μ is the x-ray attenuation coefficient in units of area per mass, and A is the pixel area in the image. With a background intensity level I_b and multiple x-ray frequencies ν passing through multiple materials i the general formula becomes:

$$I = \sum_{\nu} I_{0,\nu} \prod_{i=1,2,3,\ldots} e^{-\frac{\mu_i(\nu) m_i}{A}} + I_b. \tag{1}$$

To estimate the cloud mass, the only two materials of interest in Eq. 1 are the Al cloud material m_2 and the CRF material of the surrounding flow m_1. Other materials (e.g., blast shields in the camera protecting the detector from target debris) do not move and their contributions to x-ray attenuation is constant, so Eq. 1 can be expressed as

$$I = \sum_{\nu} I^*_{0,\nu} e^{-\frac{\mu_1(\nu) m_1}{A}} e^{-\frac{\mu_2(\nu) m_2}{A}} + I_b, \tag{2}$$

where the new coefficients $I^*_{0,\nu}$ include attenuation from m_3, m_4, ... etc. To be precise, $m_1 = m_1(m_2)$, but because the opacity of the cloud material is much larger than that of the flow material, i.e., $\mu_2(\nu) \gg \mu_1(\nu)$ for all frequencies ν, m_1 can be assumed constant, giving

$$I(m_2) = \sum_{\nu} I_{1,\nu} e^{-\frac{\mu_2(\nu) m_2}{A}} + I_b, \tag{3}$$

where $I_{1,\nu} = I^*_{0,\nu} \exp\left(-\mu_1\left(\nu\right) m_1/A\right)$.

The relative (but not absolute) strength of the non-attenuated intensities $I_{0,\nu}$ can be measured using an x-ray spectrometer, and this was done for Ti backlighters (for a type very similar to ours) by Glendinning et al. (2000). The absolute intensity $\sum\limits_{\nu} I^*_{0,\nu} + I_b$ can be measured in a portion of each image that is not occupied by the shock tube (or alternatively $\sum\limits_{\nu} I_{1,\nu} + I_b$ can be measured in unshocked material m_1). The background intensity I_b includes all sources of non-directional exposure, such as film fogging, non-directional x rays, energetic particles, etc, and can be measured if the image includes an object that is opaque to all contributions under the frequency summation; in our case this is accomplished using the Au spatial reference grid. With all the intensity coefficients known, Eq. 3 could be solved numerically for m_2. However, we will avoid a numerical iteration by making a further simplification taking advantage of our backlighter x rays being near-monochomatic; 80% is He-α at 4.7 keV (with He-β at 5.6 keV dominating the remaining 20%).

By approximating all $\mu_2\left(\nu\right)$ with the same constant value μ_2, Eq. 3 simplifies to

$$I\left(m_2\right) = I_1 e^{-\frac{\mu_2 m_2}{A}} + I_b \tag{4}$$

which can be rearranged for an expression of the mass:

$$m_2 = -\frac{A}{\mu_2} \ln\left(\frac{I - I_b}{I_1}\right), \tag{5}$$

but we have then introduced an error δI_μ in $I\left(m_2\right)$:

$$\delta I_\mu = \sqrt{\sum_\nu \left[\frac{dI}{d\mu_2\left(\nu\right)} \delta\mu_2\left(\nu\right)\right]^2} \leq \sqrt{\sum_\nu \left[I_{1,\nu} \frac{\max\left(m_2\right)}{A} e^{-\frac{\mu_2(\nu)\max(m_2)}{A}} \delta\mu_2\left(\nu\right)\right]^2} \tag{6}$$

where $\delta\mu_2\left(\nu\right) = \left|\mu_2\left(\nu\right) - \mu_2\right|$ and $\max\left(m_2\right)$ is the maximum cloud mass we would expect in any pixel [which in our case is safely estimated by a (hypothetical) pixel containing the original center point of the Al sphere]. This error is added to a measurement error δI_1 of the mean pixel value in an area of the CRF flow surrounding the cloud (an area that excludes the cone of stripped material). There is also a measurement error δI_b of the mean pixel value of the Au grid. We take both to be standard deviations and the total error in the measured mass (in any given pixel with intensity I) then becomes:

$$\delta m_2 = \sqrt{\left(\frac{\partial m_2}{\partial I_1}\right)^2 \left(\delta I_1^2 + \delta I_\mu^2\right) + \left(\frac{\partial m_2}{\partial I_b} \delta I_b\right)^2} = \frac{A}{\mu_2} \sqrt{\frac{\delta I_1^2 + \delta I_\mu^2}{I_1^2} + \frac{\delta I_b^2}{\left(I - I_b\right)^2}}. \tag{7}$$

The total error in the measured mass of the entire cloud, consisting of N pixels, then becomes:

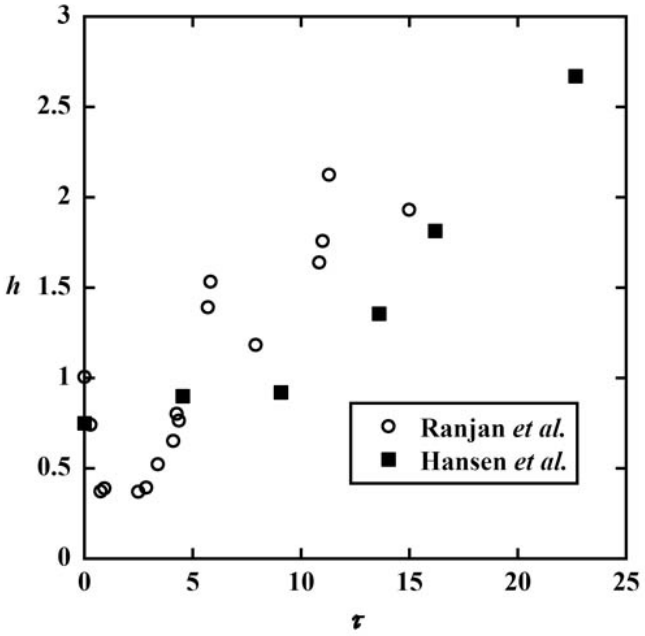

Fig. 4.— Normalized plasma height h (dimension along shocktube axis) as a function of normalized time τ for this work and compared to a recent experiment by Ranjan et al. (2005).

$$\delta m_{tot} = \frac{A}{\mu_2}\sqrt{N\frac{\delta I_1^2 + \delta I_\mu^2}{I_1^2} + \delta I_b^2 \sum_{p=1}^{N} \frac{1}{\left(I - I_b\right)^2}}. \tag{8}$$

Using an x-ray attenuation coefficient for our Al cloud material of $\mu_2 = 191.2$ cm^2/g, we then calculate the cloud mass to be 0.67 ± 0.11 μg at $t = 30$ ns and 0.54 ± 0.11 μg at $t = 40$ ns [where only 5% of the 0.11 μg total error comes from using a single attenuation coefficient μ_2, justifying our simplification of disregarding multiple x-ray frequencies]. These values can be compared to the original sphere mass of 2.44 μg.

Figures 4 and 5 show the physical dimensions, height and width, of the Al plasma cloud at different times.The quantities in these plots are normalized for comparison to recent data by Ranjan et al. (2005) from another shock-cloud interaction experiment (Ranjan et al. 2005; Niederhaus et al. 2005) where 5 cm large soap-bubbles filled with Ar is placed in a N_2 environment and shocked by planar shocks at a Mach number $M = 2.88$. In our experiment the dimensionless time $\tau = (t - 5 \text{ ns}) \times \max\left(U_\infty\right)/D_0$ where $\max\left(U_\infty\right) = 77.7$ km/s. (The 5 ns offset comes from our definition of the experimental time t starting when the laser pulse is fired, while Ranjan *et al.* defines τ from when the shock hits the cloud.) The normalized

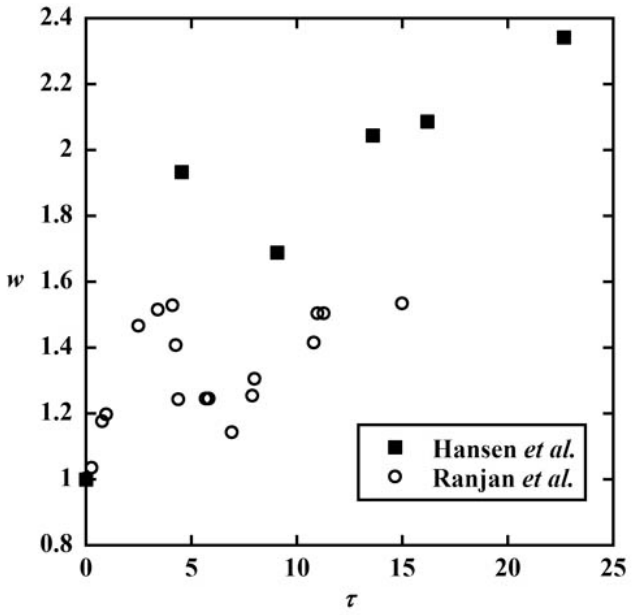

Fig. 5.— Normalized plasma width w (dimension along shocktube axis) as a function of normalized time τ for this work and compared to a recent experiment by Ranjan et al. (2005).

height h is the size of the cloud measured along the shock tube axis divided by D_0, and the width w is the size perpendicular to the the shock tube axis divided by D_0. The qualitative response of the cloud is the same in both experiments; the height is initially compressed and the width increases rapidly. At around $\tau \approx 5$ the height returns to unity while the width is noticeably reduced. This lasts until $\tau \approx 9$ when both height and width begins a gradual, roughly linear growth with time. Quantitatively we see a larger width but smaller height than Ranjan *et al.* at comparable times.

4. Analysis

We present in this section a new mathematical model that describes mass-stripping from a cloud under turbulent, high Reynolds number conditions. We compare this model to our experimental data and to an existing model (Taylor 1963; Ranger & Nicholls 1969) for laminar mass-stripping. Our model combines four separate concepts of fluid mechanics: (1) the integral momentum equations for a viscous boundary layer, (2) the equations for a potential flow past a sphere (we use potential flow with good result; for further refinement this could be changed, e.g., to Fage's equation (Fage 1936) albeit with the penalty of more complicated algebra), (3) Spalding's law of the wall for turbulent boundary layers (Spalding 1961), and (4) the skin friction coefficient for a turbulent boundary layer on a flat plate.

We begin with the integral momentum equations for a stationary, viscous boundary layer:

$$\frac{\partial}{\partial x}\int_0^{\delta_1} u_1\left(U-u_1\right)\mathrm{d}y_1 + \frac{\mathrm{d}U}{\mathrm{d}x}\int_0^{\delta_1}\left(U-u_1\right)\mathrm{d}y_1 + \frac{1}{r}\frac{\mathrm{d}r}{\mathrm{d}x}\int_0^{\delta_1} u_1\left(U-u_1\right)\mathrm{d}y_1 = \nu_1\left.\frac{\partial u_1}{\partial y_1}\right|_{y_1=0} \tag{9}$$

$$\frac{\partial}{\partial x}\int_0^{\delta_2} u_2^2\mathrm{d}y_2 + \frac{1}{r}\frac{\mathrm{d}r}{\mathrm{d}x}\int_0^{\delta_2} u_2^2\mathrm{d}y_2 + \frac{1}{\rho_2}\frac{\mathrm{d}p}{\mathrm{d}x}\delta_2 = -\nu_2\left.\frac{\partial u_2}{\partial y_2}\right|_{y_2=0} \tag{10}$$

$$\rho_1\nu_1\left.\frac{\partial u_1}{\partial y_1}\right|_{y_1=0} = -\rho_2\nu_2\left.\frac{\partial u_2}{\partial y_2}\right|_{y_2=0} \tag{11}$$

where x is a coordinate along the surface of the cloud (we will approximate the cloud with a sphere at all times so that $x = 0$ at the flow stagnation point and $x = \frac{\pi}{2}R$ at the equator), y is a coordinate perpendicular to the cloud surface, r is the distance from the cloud surface to the cloud axis of symmetry, $U = U\left(x\right)$ is the free stream flow velocity behind the shock,

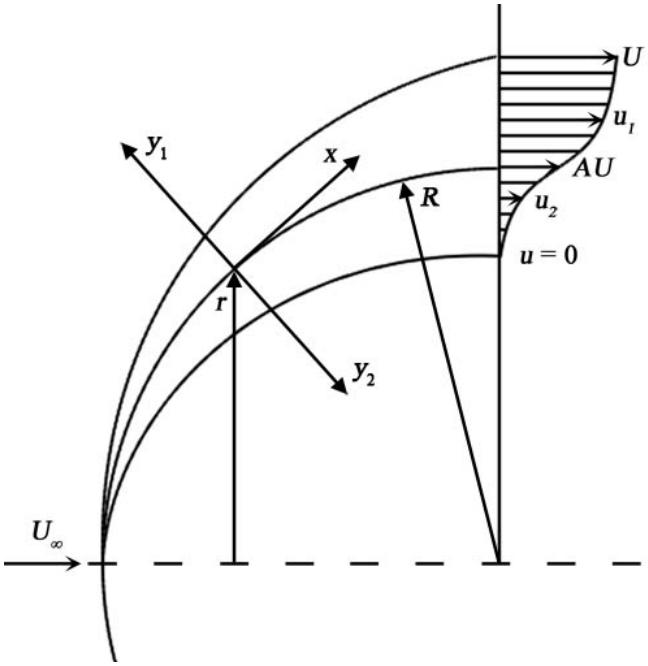

Fig. 6.— The flow geometry around the cloud is modelled with the potential flow around a sphere with the boundary layer flow calculated using a local cartesian coordinate system where the coordinate x is along the flow (i.e., along the surface of the sphere) and y is the distance into the boundary layer from the sphere surface. The velocity in the boundary layer is u_1 outside the sphere radius R and u_2 inside the sphere radius. At the outside edge of the boundary layer $y_1 = \delta_1$ the velocity $u_1 = U$, i.e., matches the potential flow velocity. At the sphere radius $u_1 = u_2 = AU$, where A is a constant. At the inside edge of the boundary layer $y_2 = \delta_2$ the velocity $u_2 = 0$. The cylindrical coordinate r is the distance from the axis of symmetry to the sphere surface.

$u = u(x, y)$ is the flow velocity inside the boundary layer, ν is the kinematic viscosity, ρ is the density, $p = p(x)$ is the pressure, and $\delta = \delta(x)$ is the thickness of the boundary layer. The flow properties U, u, ν, ρ, p, and δ are also functions of time t, but are changing relatively slowly (the flow is changing at a timescale which is longer than the transit time past the cloud) and so we have chosen to use the equations for a stationary boundary layer to make the problem more tractable. Subscript 2 denotes plasma in the cloud and subscript 1 the surrounding flow, e.g., δ_2 is the boundary layer thickness inside the cloud. The geometry is sketched out in Fig. 6.

Taylor (1963) developed a theory for wind stripping the surface layer of a fluid, and subsequently Ranger & Nicholls (1969) extended Taylor's model to estimate how much mass

is stripped from falling raindrops. Taylor's theory is laminar, and while it works beautifully for raindrops, i.e., for low Mach and Reynolds numbers, we will see below that it does not accurately predict mass-stripping under turbulent high Reynolds number conditions. However, we follow Taylor's lead in relating the flow velocity on the surface of the cloud to the free stream flow velocity through the expression AU where A is a constant, as indicated in Fig. 6. Inside the boundary layer, away from the surface in either direction, our expressions will become more complicated than Taylor's, who assumes *ad hoc* relations for the flow velocities inside the boundary layers, $u_1/U = 1 - (1 - A)\exp\left(-y_1/\alpha_1 x^p\right)$ and $u_2/U = A\exp\left(-y_2/\alpha_2 x^p\right)$, where Taylor sets $p = 1/2$ and solves the system of equations for the coefficients α_1, α_2, and A. Instead of these arbitrary expressions for the velocities u_1 and u_2, we will use Spalding's law of the wall for turbulent boundary layers (Spalding 1961):

$$y^+ = u^+ + e^{-\kappa B}\left(e^{\kappa u^+} - 1 - \kappa u^+ - \frac{\left(\kappa u^+\right)^2}{2} - \frac{\left(\kappa u^+\right)^3}{6}\right) \tag{12}$$

an empirical relation that has been shown to hold in countless fluid dynamics experiments and a multitude of regimes. Here, the dimensionless coordinate $y^+ \equiv yv^*/\nu$ and the dimensionless velocity $u^+ \equiv u/v^*$, or in the appropriate coordinate frame of reference $u_1 = v_1^* u_1^+ + AU$ and $u_2 = AU - v_2^* u_2^+$. Here, the wall-friction velocity v^* is defined through $v^{*^2} = \nu\left(\mathrm{d}u/\mathrm{d}y\right)\big|_{y=0}$ and Coles (1955) gives the coefficients $\kappa = 0.41$ and $B = 5.0$ [using the values $\kappa = 0.4$ and $B = 5.5$ given by Nikuradse (1930) does not produce significantly different results].

Next we shall proceed by carrying out the spatial derivatives with respect to x as far as we can in Eqs. 9 and 10. To reduce the algebra we will assume that the free stream velocity around the cloud follows the potential flow of a sphere,

$$U\left(x\right) = \frac{3}{2}U_\infty \sin\left(\frac{x}{R}\right), \tag{13}$$

where U_∞ is the flow velocity far from the sphere, and we shall assume U_∞ to be uniform over the dimension of the cloud (this is very nearly true in the experiment). One could certainly use a non-uniform flow field, e.g., $U_\infty\left(x\right) = U_\Lambda\left(1 + \Lambda_1 \cos\left(x/R\right)\right)$ where the numerical constant Λ_1 is negative for a decelerating flow field, or a different expression for the free stream velocity, e.g., Fage's (Fage 1936) equation $U/U_\infty = 1.5x/R - 0.4371\left(x/R\right)^3 + 0.1481\left(x/R\right)^5 - 0.0423\left(x/R\right)^7$, but the potential flow expression has the advantage that $\mathrm{d}U/\mathrm{d}x = 0$ at the equator $x = \pi R/2$, which will simplify the algebra substantially. Also, at the equator $\mathrm{d}p/\mathrm{d}x = -\rho_g U \mathrm{d}U/\mathrm{d}x = 0$ and trivially $\mathrm{d}r/\mathrm{d}x = 0$. Carrying out the spatial derivative and setting $x = \pi R/2$ we then find that Equation 9 becomes:

$$\int_0^{\delta_1} v_1^{'*} u_1^+ \left[(1-2A)\, U - 2 v_1^* u_1^+ \right] \mathrm{d}y_1 = v_1^{*^2} \tag{14}$$

where $v_1^{'*} = \mathrm{d}v_1^*(x)/\mathrm{d}x$ and $U = 3U_\infty/2$. Equation 10 becomes:

$$\int_0^{\delta_2} 2 v_2^{'*} u_2^+ \left(v_2^* u_2^+ - AU \right) \mathrm{d}y_2 = v_2^{*^2}. \tag{15}$$

Next we will carry out the integration with respect to y. This is done by substituting $\mathrm{d}u^+$ for $\mathrm{d}y$ using Spalding's law of the wall (Eq. 12) and noting that when $y = \delta$ then $u_1^+ = (1-A)\, U/v_1^*$ in the CRF and $u_2^+ = AU/v_2^*$ in the Al cloud. Integrating Eq. 14 we then obtain

$$\begin{aligned} v_1^{'*}\nu_1 \Bigg[& -\frac{1}{6}\left(1-\kappa e^{-\kappa B}\right)(1+2A)(1-A)^2 \left(\frac{U}{v_1^*}\right)^3 + \frac{1}{6}\kappa^2 e^{-\kappa B}(1+A)(1-A)^3 \left(\frac{U}{v_1^*}\right)^4 + \\ & + \frac{1}{40}\kappa^3 e^{-\kappa B}(3+10A)(1-A)^4 \left(\frac{U}{v_1^*}\right)^5 + \frac{1}{\kappa} e^{-\kappa B}(1-2A)\frac{U}{v_1^*}\left(e^{\kappa \frac{U}{v_1^*}(1-A)} \left(\kappa \frac{U}{v_1^*}(1-A) - 1 \right) + 1 \right) + \\ & - 2\frac{1}{\kappa^2} e^{-\kappa B} \left(e^{\kappa \frac{U}{v_1^*}(1-A)} \left(\left(\kappa \frac{U}{v_1^*}(1-A) \right)^2 - 2\kappa \frac{U}{v_1^*}(1-A) + 2 \right) - 2 \right) \Bigg] = v_1^{*^2} \end{aligned} \tag{16}$$

Integrating Eq. 15 gives

$$\begin{aligned} 2v^{'*}\nu_2 \Bigg[& -\frac{1}{6}\left(1-\kappa e^{-\kappa B}\right) \left(\frac{AU}{v_2^*}\right)^3 + \frac{1}{12} e^{-\kappa B}\kappa^2 \left(\frac{AU}{v_2^*}\right)^4 + \frac{1}{40} e^{-\kappa B}\kappa^3 \left(\frac{AU}{v_2^*}\right)^5 + \\ & - \frac{1}{\kappa} e^{-\kappa B} \frac{AU}{v_2^*} \left(e^{\frac{\kappa AU}{v_2^*}} \left(\frac{\kappa AU}{v_2^*} - 1 \right) + 1 \right) + \\ & + \frac{1}{\kappa^2} e^{-\kappa B} \left(e^{\frac{\kappa AU}{v_2^*}} \left(\left(\frac{\kappa AU}{v_2^*} \right)^2 - 2\frac{\kappa AU}{v_2^*} + 2 \right) - 2 \right) \Bigg] = v_2^{*^2}. \end{aligned} \tag{17}$$

This is as far as we can go without saying something about the wall-friction velocity v^*, or equivalently the skin-friction coefficient C_f, as the two are related through

$$v^{*^2} = \frac{1}{2} C_f(x)\, U^2(x). \tag{18}$$

For calculations of skin-friction drag, many researchers, beginning with Dryden & Kuethe (1930) and Millikan (1932), have used velocity distributions for a flat plate in non-flat geometries and found that the results do not differ seriously from measured values (Goldstein 1965). We will do the same and use the skin friction coefficient for a turbulent boundary layer on a flat plate (White 1974):

$$C_f(x) \approx 0.0592\,\mathrm{Re}_x^{-1/5} \tag{19}$$

where the Reynold's number $\mathrm{Re}_x = Ux/\nu$, but with a modification; if we use Eq. 19 as is, the problem is overdetermined. We need to introduce the equivalent of Taylor's α_1 and α_2. For very small u^+ we have

$$y = \frac{\nu}{v^*}\left[\frac{u}{v^*} + e^{-\kappa B}\left(e^{\kappa u^+} - 1 - \kappa u^+ - \frac{\left(\kappa u^+\right)^2}{2} - \frac{\left(\kappa u^+\right)^3}{6}\right)\right] \sim \frac{\nu u}{v^{*2}} = \frac{2\nu u}{C_f(x)\,U^2(x)}. \tag{20}$$

Comparing this to Taylor's

$$y_2 = -\alpha_2 x^p \ln\frac{u_2}{AU}$$

suggests that we should replace the coefficient 0.0592 with a coefficient that will be determined by our system of equations. We set:

$$C_f(x) = \frac{2}{\alpha^2}\left(Ux/\nu\right)^{-1/5}. \tag{21}$$

which allows us to calculate the spatial derivative of v^* as

$$v'^*(x) = -\frac{1}{10}\frac{v^*}{x}. \tag{22}$$

In the CRF at the equator $x = \pi R/2$ we then get

$$\frac{U}{v_1^*} = \left(\frac{3\pi U_\infty R}{4\nu_1}\right)^{1/10}\alpha_1 = K_1\alpha_1 \tag{23}$$

where we have defined a new coefficient K_1 that depends only on known quantities, and we can rewrite Eq. 16 as

$$\begin{aligned}1200\kappa^2 e^{\kappa B}K_1^9\left(1-A\right)\alpha_1^{-1} = 120e^{\xi}\left[\left(1+2A\right)\xi^2 - \left(3+2A\right)\xi + 4\right] - 3\left(3+10A\right)\xi^5 + \\ - 20\left(1+A\right)\xi^4 + 20\left(\kappa^{-1}e^{\kappa B} - 1\right)\left(1+2A\right)\xi^3 - 120\left(1-2A\right)\xi - 480\end{aligned} \tag{24}$$

where

$$\xi = \kappa K_1 (1 - A) \alpha_1. \tag{25}$$

We expect A to be a fairly small quantity because of the difference in densities between cloud and surrounding flow (it will certainly be smaller than unity) so one might be tempted to linearize Eq. 24 w.r.t. A, but this only simplifies terms where A (or ξ) does not appear in the exponents and does not lead to an analytical solution for A as it does in the laminar theory. Consequently some form of simple numerical scheme must be employed to calculate A, and we have therefore chosen to not linearize Eq. 24 w.r.t. A, but to keep the exact form.

Similarly in the Al cloud defining

$$K_2 = \left(\frac{3\pi U_\infty R}{4\nu_2} \right)^{1/10} \tag{26}$$

allows us to rewrite Eq. 17 as

$$600\kappa^2 e^{\kappa B} K_2^9 \alpha_2^{-1} = 120 e^\eta (\eta - 2) - 3\eta^5 - 10\eta^4 + 20 \left(\frac{1}{\kappa} e^{\kappa B} - 1 \right) \eta^3 + 120\eta + 240 \tag{27}$$

where

$$\eta = \kappa K_2 A \alpha_2. \tag{28}$$

Next relate α_1 to α_2 by rewriting Eq. 11 as

$$\alpha_1 = K_3 \alpha_2 \tag{29}$$

where

$$K_3 = \left(\frac{\rho_1}{\rho_2} \right)^{1/2} \left(\frac{\nu_1}{\nu_2} \right)^{1/10}. \tag{30}$$

We eliminate α_1 by substituting Eq. 29 in Eqs. 24-25, leaving us with two equations, Eqs. 24 and 27, for two unknown coefficients A and α_2. This equation pair can easily be solved numerically, e.g., Eq. 24 can be solved for A by simple iteration as it converges rapidly, and a simple regula falsi (secant) method can be used for Eq. 27, but other numerical schemes will work, too, and we used a globally convergent Newton's method. With A and α_2 at hand, one easily calculates the mass stripped from the cloud by integrating the cloud material flowing through the boundary layer at the equator (Ranger & Nicholls 1969):

$$\frac{\mathrm{d}m}{\mathrm{d}t} = 2\pi R \rho_2 \int_0^{\delta_2} u_2 \mathrm{d}y_2 = 2\pi R \rho_2 \nu_2 \psi (\eta) \tag{31}$$

where we have defined a mass-strip coefficient

$$\psi(\eta) = \frac{1}{2\kappa^2}\eta^2 + \frac{1}{\kappa}e^{-\kappa B}\left(1 - \eta - \frac{1}{2}\eta^2 - \frac{1}{6}\eta^3 - \frac{1}{24}\eta^4 + e^{\eta}\right). \quad (32)$$

It should be noted that $\mathrm{d}m/\mathrm{d}t$ is *not* proportional to R, ρ_2, or ν_2 because $\eta = \eta(R, U_\infty, \rho_1, \rho_2, \nu_1, \nu_2)$ from the numerical solution above.

Using the specific physical quantities for our experiment, we can now calculate the mass stripped as a function of time and compare the calculation to our experimental data. For the cloud radius $R(t)$ we use measured values from the experiment images, namely half of the measured width in Fig. 5, and interpolate to other times. For values of the free stream flow velocity $U_\infty(t)$, the density $\rho_1(t)$, and the temperature $T(t)$, we use values from HYADES. The density $\rho_2(t)$ is obtained by applying the same compression as for $\rho_1(t)$. Additionally, the peak compressions are independently verified from the experiment at $t = 5$ ns where the left side of the sphere is compressed to an ellipsoid shape with minor radius ~ 30 μm, corresponding to a compression of ~ 4 (which is the strong shock limit for a polytropic gas with adiabatic index $\gamma = 5/3$).

With our given physical quantities, the coefficients $K_1 \approx 5$, $K_2 \approx 3$, and $K_3 \approx \frac{1}{4}$ at all times. From solving Eqs. 24, 27 and 29 we calculate the coefficients $A \approx 1/5$, $\alpha_1 \approx 6$, and $\alpha_2 \approx 27$ at all times, and we find that the compound quantity η varies between $4 \lessapprox \eta \lessapprox 8$ (except very briefly when the rarefaction changes the direction of the flow) so that the mass-strip coefficient ψ is in the range $4 \times 10^2 \lessapprox \psi \lessapprox 4 \times 10^3$. The mass of the cloud as a function of time is plotted in Fig. 7and reaches $m = 0$ (fully stripped) by $t \approx 90$ ns. This agrees well with the experiment where the cloud can no longer be observed by 80 ns-100 ns. By comparison, the equivalent mass-strip coefficient $\psi = (2\pi R \rho_l \nu_l)^{-1}\,\mathrm{d}m/\mathrm{d}t$ in the laminar theory is $\lessapprox 4 \times 10^2$ for all times of interest in the experiment, which is too low to achieve the cloud being completely stripped by $t \approx 80$ ns; if the mass-stripping was done by laminar flow and continued under the same conditions past $t = 80$ ns (ignoring experimental limitations) the laminar mass-stripping time would be ~ 1 μs. As a final note, to illustrate the non-linearity between $\mathrm{d}m/\mathrm{d}t$ and the various physical quantities one can arbitrarily double, say, the value of the viscosity ν_2 and see that this leads to only a 12% increase in $\mathrm{d}m/\mathrm{d}t$.

5. Conclusions

We observe the rapid stripping of all mass from a simulated interstellar cloud in a laser experiment. We present a model that agrees very well with our experimental observations. The model combines (1) the integral momentum equations for a viscous boundary layer, (2) the equations for a potential flow past a sphere, (3) Spalding's law of the wall for turbulent

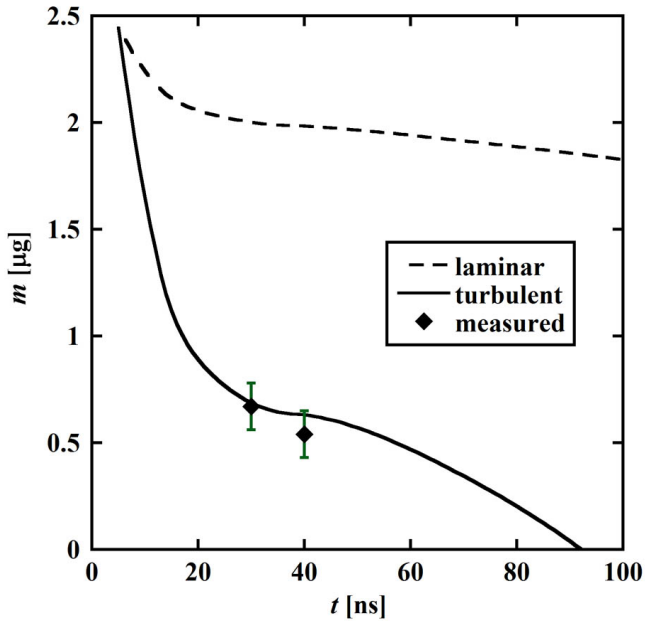

Fig. 7.— Cloud mass remaining as a function of time calculated using a laminar model (Taylor 1963; Ranger & Nicholls 1969) (dashed line) and the turbulent model presented in this manuscript (solid line), compared to experimentally measured values of the cloud mass (two squares). The turbulent model agrees with the measured values and also predicts that the cloud is completely stripped by $\sim$ 90 ns, which compares well with the experimental observation of the cloud being stripped by 80 ns-100 ns. In the laminar model (assuming unchanged condition from 80 ns) the cloud is not stripped until $\sim$ 1 μs.

boundary layers, and (4) the skin friction coefficient for a turbulent boundary layer on a flat plate. By comparison, a laminar model overestimates the stripping time by an order of magnitude. This suggests that mass-stripping in the experiment must be of a turbulent nature, and with its even higher Reynolds numbers, this must hold also in the astrophysical case. This suggests that the relatively short life times of interstellar clouds may be due to shock-cloud interactions, where mass is stripped from a boundary layer on the cloud surface by passing shocks and subsequent high Reynolds number flows.

We would like to thank C. F. McKee, Departments of Physics and Astronomy, University of California, Berkeley for his support of this project.

This work was performed under the auspices of the U. S. Department of Energy by the University of California, Lawrence Livermore National Laboratory under Contract No. W-7405-Eng-48.

REFERENCES

Barton, R. T. 1985, in Numerical Astrophysics, ed. J. M. Centrella, J. M. LeBlanc, and R. L. Bowers (Jones and Bartlett, Boston), 482–497

Bedogni, R., & Woodward, P. R. 1990, Astron. and Astrophys., 231, 481

Boehly, T. R., Brown, D. L., Craxton, R. S., Keck, R. L., Knauer, J. P., Kelly, J. H., Kessler, T. J., Kumpan, S. A., Loucks, S. J., Letzring, S. A., Marshall, F. J., McCrory, R. L., Morse, S. F. B., Seka, W., Soures, J. M., & Verdon, C. P. 1997, Optics Communications, 133, 495

Budil, K. S., Perry, T. S., Bell, P. M., Hares, J. D., Miller, P. L., Peyser, T. A., Wallace, R., Louis, H., & Smith, D. E. 1996, Rev. Sci. Inst., 67, 485

Byun, D. Y., Koo, B. C., Tatematsu, K., & Sunada, K. 2006, Astrophys. J., 637, 283

Clark, P. C., & Bonnell, I. A. 2005, Mon. Not. R. Astron. Soc., 361, 2

Clérouin, J. G., Cherfi, M. H., & Zérah, G. 1998, Europhys. Lett., 42, 37

Coles, D. E. 1955, in Fifty Years of Boundary Layer Research, ed. W. Tollmien and W. Görtler (Vieweg, Brunswick), 133

Cowie, L. L., McKee, C. F., & Ostriker, J. P. 1981, Astrophys. J., 247, 908

Dryden, H. L., & Kuethe, A. M. 1930, N.A.C.A. Report, 342, 12

Fage, A. 1936, Aeronaut. Res. Council Lond., RM-1766

Fragile, P. C., Murray, S. D., Anninos, P., & van Breugel, W. 2004, Astrophys. J., 604, 74

Glendinning, S. G., Colvin, J., Haan, S., Kalantar, D. H., Landen, O. L., Marinak, M. M., Remington, B. A., Wallace, R., Cherfils, C., Dague, N., Divol, L., Galmiche, D., & Richard, A. L. 2000, Phys. Plasmas, 7, 2033

Goldstein, S., ed. 1965, Modern Developments in Fluid Dynamics (Dover, New York)

Hartmann, L., Ballesteros-Paredes, J., & Bergin, E. A. 2001, Astrophys. J., 562, 852

Hartquist, T. W., Dyson, J. E., Pettini, M., & Smith, L. 1986, Mon. Not. R. Astron. Soc., 221, 715

Heathcote, S. R., & Brand, P. W. J. L. 1983, Mon. Not. R. Astron. Soc., 203, 67

Hwang, U., Flanagan, K. A., & Petre, R. 2005, Astrophys. J., 635, 355

Klein, R. I., Budil, K. S., Perry, T. S., & Bach, D. R. 2000, Astrophys. J. Suppl. S., 127, 379

—. 2003, Astrophys. J., 583, 245

Klein, R. I., McKee, C. F., & Colella, P. 1994, Astrophys. J., 420, 213

Larsen, J. T., & Lane, S. M. 1994, J. Quant. Spectrosc. Radiat. Transfer, 51, 179

Larson, R. B. 1981, Mon. Not. R. Astron. Soc., 194, 809

Marcolini, A., Strickland, D. K., D'Ercole, A., Heckman, T. M., & Hoopes, C. G. 2005, Mon. Not. R. Astron. Soc., 362, 626

Miceli, M., Bocchino, F., Maggio, A., & Reale, F. 2005, Astron. and Astrophys., 442, 513

Miles, A. R., Braun, D. G., Edwards, M. J., Robey, H. F., Drake, R. P., & Liebrandt, D. R. 2004, Phys. Plasmas, 11, 3631

Millikan, R. A. 1932, Trans. Amer. Soc. Mech. Engineers, 54, 29

More, R. M., Warren, K. H., Young, D. A., & Zimmerman, G. B. 1988, Phys. Fluids, 31, 3059

Niederhaus, J., Ranjan, D., Anderson, M., Oakley, J., Bonazza, R., & Greenough, J. 2005, Fusion Sci. Technol., 47, 1160

Nikuradse, J. 1930, Ing.-Arch., 1, 306

Nittmann, J., Falle, S. A. E. G., & Gaskell, P. H. 1982, Mon. Not. R. Astron. Soc., 201, 833

Padoan, P., Juvela, M., Goodman, A. A., & Nordlund, Å. 2001, Astrophys. J., 553, 227

Palla, F., & Stahler, S. W. 2000, Astrophys. J., 540, 255

Patnaude, D. J., & Fesen, R. A. 2005, Astrophys. J., 633, 240

Ranger, A. A., & Nicholls, J. A. 1969, AIAA Journal, 7, 285

Ranjan, D., Anderson, M., Oakley, J., & Bonazza, R. 2005, Phys. Rev. Lett., 94, 184507

Robey, H. F. 2004, Phys. of Plasmas, 11, 4123

Robey, H. F., Perry, T. S., Klein, R. I., Kane, J. O., Greenough, J. A., & Boehly, T. R. 2002, Phys. Rev. Lett., 89, 085001

Ryutov, D., Drake, R. P., Kane, J., Liang, E., Remington, B. A., & Wood-Vasey, W. M. 1999, Astrophys. J., 518, 821

Smith, L. J., Pettini, M., Dyson, J. E., & Hartquist, T. W. 1984, Mon. Not. R. Astron. Soc., 211, 679

Spalding, D. B. 1961, J. Appl. Mech., 28, 455

Taylor, G. I. 1963, The Shape and Acceleration of a Drop in a High Speed Air Stream. In the Scientific Papers of G. I. Taylor, ed. G. K. Batchelor (University Press, Cambridge)

White, F. M. 1974, Viscous Fluid Flow (McGraw-Hill, New York)

Widnall, S. E., Bliss, D. B., & Tsai, C. 1974, J. Fluid Mech., 66, 35

Woodward, P. R. 1976, Astrophys. J., 207, 484